Applied Surface Science 609 (2023) 155317

Contents lists available at ScienceDirect

Applied Surface Science

journal homepage: www.elsevier.com/locate/apsusc

Full Length Article

Assessing advanced methods in XPS and HAXPES for determining the thicknesses of high-*k* oxide materials: From ultra-thin layers to deeply buried interfaces

T.R. Bure [a,*], O. Renault [a], E. Nolot [a], T. Lardin [a], C. Robert-Goumet [b], N. Pauly [c]

[a] Univ. Grenoble-Alpes, CEA, Leti, 38000 Grenoble, France
[b] Université Clermont Auvergne, Clermont Auvergne INP, CNRS, Institut Pascal, F-63000 Clermont-Ferrand, France
[c] Université Libre de Bruxelles, Service de Métrologie Nucléaire (CP 165/84), 50 av. F. D. Roosevelt, B-1050 Brussels, Belgium

ARTICLE INFO

Keywords:
Hard X-ray photoelectron spectroscopy (HAXPES)
Inelastic background analysis
Angle-resolved X-ray photoelectron spectroscopy (ARXPS)
High-*k* materials
Buried layers
Atomic layer deposition (ALD)

ABSTRACT

We assess advanced XPS-based methods in determining depth distribution in alumina and hafnia ALD samples of increasing thicknesses and buried layer depths. First, dose quantification of Al in ultrathin alumina is achieved through non-destructive wavelength dispersive X-ray fluorescence (WDXRF), which is confirmed by comparison to destructive liquid-phase deposition inductively coupled plasma mass spectrometry (LPD-ICPMS) (uncertainty 10 %). Second, we compare WDXRF to parallel ARXPS (pARXPS) in precise dose and thickness quantification in ultrathin alumina, and present the ability of pARXPS to accurately track linear growth during the deposition. Thickness determination of an intermediate ALD stack of silicon dioxide, hafnia, and alumina layers of 1–2 nm by pARXPS is evaluated against quantitative, reference-free grazing incidence X-ray fluorescence (GIXRF) (uncertainty 8–9 %). An alternative technique employing inelastic background analysis (IBA) is introduced as a fast and accurate method and subsequently compared with pARXPS and GIXRF thickness determinations. Finally, in thicker multilayer systems, hard X-ray photoelectron spectroscopy (HAXPES) combined with IBA is proposed for an in-depth analysis for thicknesses up to 28 nm, with generated interface locations and layer thicknesses well-aligned to nominal values. This study is a novel application of lab-based Cr-Kα HAXPES spectra for inelastic background analysis in thick metal-oxide multilayer materials.

1. Introduction

Dielectrics are pressed to meet ever-mounting requirements for high dielectric strength, high permittivity, low dielectric loss, and high tunability in a wide frequency range [1,2]. These properties are universally valued across nanoelectronics in memory devices, gate insulators, energy storage, and high frequency devices [1,3], where different dielectric materials and different layer thicknesses, in the sub-nm to tens of nm range, are needed depending on the final application. The extremely stable and robust alumina (Al_2O_3) is a classic favorite in memory device technology, and has been integrated into nanoelectronics' dielectric configurations. Demonstrating a high band gap, thermodynamic stability on Si, and amorphous structure in the conditions of interest, it promises high relative permittivity and high breakdown voltage. Hailing from use in optical coating and DRAM applications, hafnia (HfO_2) is similarly promising, reaching low leakage currents at increased thicknesses relative to SiO_2 [2,4]. Al_2O_3 and HfO_2 have been studied as bilayer systems for dielectrics with increased charge storage capacity. It was found that the thicknesses of the sub-layers affected the interface and resulting physical properties. Therefore, their precise control is imperative to the desired functionality of the device [5]. Furthermore, the dielectric properties of Al_2O_3 are influenced by its crystal structure. The structure is highly variable and is ordered according to the deposition conditions [2].

An exacting demand for certain material specifications drives progress in the fabrication processes, which then enables greater control and tuning of material properties. Atomic layer deposition (ALD) permits atomic level control of thin film deposition, and thus scaling in the nanodevice. The chemical mechanism of ALD sees the precursor and co-reactant reacting in two vapor phases for each ALD cycle. These reactions are self-limiting, ensuring conformity in the layer and monolayer growth [2,6,7]. At every stage of the deposition process, the exact

* Corresponding author.
E-mail address: taylor.bure@cea.fr (T.R. Bure).

https://doi.org/10.1016/j.apsusc.2022.155317
Received 21 February 2022; Received in revised form 4 October 2022; Accepted 12 October 2022
Available online 17 October 2022

location of the buried interfaces should be known without disrupting the interfacial phenomena [1]. Different X-ray characterization techniques offer a non-invasive solution with high accuracy, and have been widely integrated into fabrication lines in the cleanroom [8–10]. X-ray reflectivity (XRR), X-ray fluorescence (XRF), and parallel angle-resolved X-ray photoelectron spectroscopy (pARXPS) are some of the more common approaches [9–13]. X-ray photoelectron spectroscopy (XPS) is a surface sensitive method, but it can be further mined for depth information by analyzing the inelastic background following the peak using the Tougaard method of inelastic background analysis (IBA) [14,15]. Moreover, hard X-ray photoelectron spectroscopy (HAXPES) permits profound depth information, and is being integrated at the lab-scale. The optimized combination of these techniques and analytical methods allows thickness determinations at the desired level of accuracy along with chemical analysis, shedding new light on the characterization of critical buried interfaces even under thick overlayers [16–18].

This work assesses the non-destructive XPS methods discussed above for the accurate compositional depth profiling of Al_2O_3 and HfO_2 high dielectric constant materials prepared by the ALD method. Monolayers and bilayers with thicknesses in the 1–28 nm range were prepared. Non-destructive X-ray techniques (i.e. WDXRF, pARXPS, XPS, and HAXPES) are used to probe these materials. WDXRF is proposed as a comparable alternative for chemical quantification of the highly calibrated liquid-phase deposition inductively coupled plasma mass spectrometry (LPD-ICPMS) which is disadvantaged by destructive and time-intensive analyses. Further, pARXPS is introduced as a non-destructive analysis which is well-fitted to ultrathin Al_2O_3 samples, and is later compared to XPS-IBA in a multilayer sample. Both methods are verified against reference-free GIXRF. Finally, IBA-HAXPES using a Cr Kα source is implemented at the lab-scale for the first time, performing the depth profiling of bilayers in which a thin metal oxide layer is buried under a thick overlayer. Please note that a glossary of terms is included at the end of the article.

2. Experimental

2.1. Sample preparation

Layers of Al_2O_3 and HfO_2 with individual thicknesses in the sub-nanometer to 25 nm range were deposited on 300 mm silicon (0 0 1) wafers by ALD. The layer thickness is determined by the number of ALD cycles. Water vapor was used as the oxygen source for both metal-oxides, while Trimethylaluminium and $HfCl_4$ were used as precursors. The deposition temperature was 300 °C. Three classes of ALD samples are examined in this work, and are presented in Fig. 1: (a) ultrathin samples of Al_2O_3 with sub-nanometer thicknesses, (b) a stack of SiO_2, HfO_2, and Al_2O_3 layers of 1–2 nm, (c) thin buried Al_2O_3 or HfO_2 layers underneath a thick layer (9–25 nm) of HfO_2 or Al_2O_3, respectively. The samples from the first class were deposited either over the native oxide, or after HF surface preparation. The sample in the second class was prepared according to the experimental specifications found in *Hönicke's* work [10]. A 1 nm chemical oxide was formed prior to the HfO_2 ALD layer deposition. The third class of ALD samples used HF surface preparation, and features two sets of three bilayer samples in which a HfO_2 or Al_2O_3 overlayer of approximately 10, 15, and 25 nm was deposited over an approximately 2.5 nm layer of either Al_2O_3 or HfO_2, respectively.

2.2. Measurement techniques

XPS measurements (PHI 5000 VersaProbe II) were using monochromated Al-Kα radiation and a takeoff angle of 45° at a pass energy of 117 eV. The FWHM for Ag $3d_{7/2}$ is 1.5 eV for this pass energy. The analyses were done with and without surface preparation by argon gas-cluster ion beam (GCIB) with a cluster size of 2500 atoms at 10 keV for 4 eV per atom of argon and a dose of 1.25nA per mm^2.

HAXPES measurements were acquired using an X-ray monochromated Cr-Kα source ($h\nu = 5414.9$ eV) as excitation and an analyzer pass energy of 280 eV, provided by the PHI Quantes instrument. The FWHM for Ag $3d_{7/2}$ is 2.3 eV for this pass energy. The photoelectron emission angle (sample-analyzer angle) was varied between 30° − 80°. The spectra were recorded over an extended energy range suitable for inelastic background analysis (IBA). The spectra included Al 1s at 1559.6 eV BE, Hf 3d at 1662 eV BE, and Si 1s at 1839 eV BE in the high binding energy region, and O 1s at 531 eV BE in the low binding energy region. Additional scans were taken in the 518 eV kinetic energy region in order to record the O KLL Auger signal for IBA.

p-ARXPS analyses were carried out with a Thermo Scientific Theta 300 spectrometer using a monochromatic Al Kα source (1486.6 eV). The two-dimensional detector at the output plane has photoelectron energy dispersed in one direction and the angular distribution dispersed in the other direction [19]. Such arrangement provides an angular range of ~60° (from 20° to 78° relative to the normal of the sample) with a resolution close to 1°. High-resolution spectra were collected using an analysis area of ~ (400 μm)^2 and a 40 eV pass energy. The energy resolution was 0.45 eV as determined from the Fermi cutoff of a gold reference sample.

p-ARXPS data were analyzed using Thermo Avantage software (version 5.9902), more specifically using the sharp interfaces multi-overlayer model. A 20-60° angular range was used in order to get rid of the contributions of elastic interactions.

Wavelength-dispersive X-ray fluorescence (WDXRF) analysis were performed on Rigaku AZX400 tool operated with Rhodium anode. We used Al-Kα and Hf-Mα lines and fundamental parameter method calibrated against Al and Hf pure targets to evaluate the deposited mass of Al and Hf. This technique has already demonstrated 1 % accuracy for ultrathin films [20]. The layer thickness was then determined based on assumptions on the material stoichiometry (HfO_2, Al_2O_3) and mass density (9.6 and 3.9 g/cc resp.).

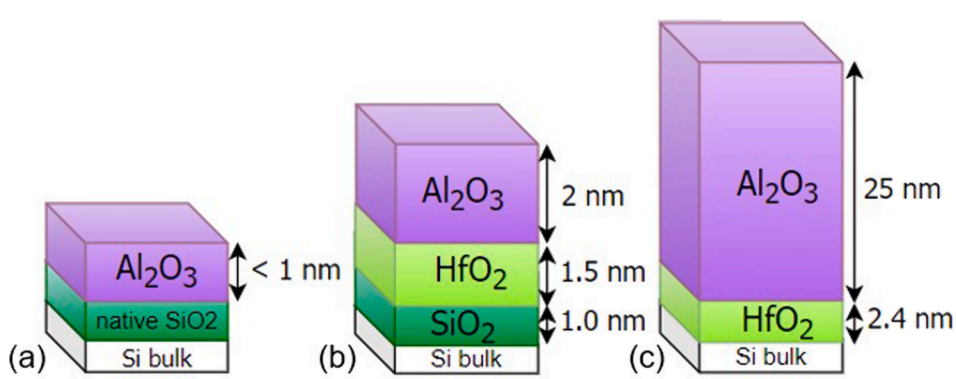

Fig. 1. The schematic representation of the structure of (a) the sub-nanometer ultrathin class of samples (with or without native oxide); (b) trilayer of thin metal oxide layers and (c) bilayers with deeply buried layer of HfO_2 or Al_2O_3 and overlayer of approximately 10, 15, and 25 nm composed of the opposing metal-oxide.

X-ray reflectometry was performed on Bruker D8 Fabline tool operated with monochromatic Cu Kα radiation. The thickness, mass density and roughness of the layers were evaluated with Bruker Leptos 7 software.

LPD-ICPMS (Liquid Phase Decomposition coupled to Inductively Coupled Plasma Mass Spectrometry) was used as a destructive, whole surface and reference technique since calibrated with certified standards for the quantification of Al dose. For chemical collection, home-made LPD system and.

VPD reactor was used. Droplet collection was carried out manually. A diluted HF solution was selected as collection solution for LPD. Analysis was performed with an Agilent ICPMS7500cs.

$$Al_2O_3 + 6\ HF \rightarrow 2\ Al^{3+} + 6F^- + 3\ H_2O$$

2.3. Inelastic background analysis

Inelastic background analysis (IBA) of the photoemission spectra was effectuated using the QUASES-Analyze software from the QUASES-Tougaard software package [21]. IBA is a well-established technique for an accurate quantification of layered and nanostructured samples in photoelectron spectroscopy, which in a number of cases suffer from non-homogeneous elemental in-depth distributions which affects the quantification accuracy relying only on the core-level peak intensity. Initially developed for XPS [22], it has been extended in the recent years to HAXPES first with an implementation of synchrotron sources [23–27] later using both synchrotron and high-energy, lab-scale Ga Lα excitation ($h\nu = 9250$ eV) [28]. IBA method affords probing depths up to 8 × IMFP [29]. In this work, IBA for the thick sample set were performed on HAXPES spectra obtained from lab-scale Cr Kα source. The method, when combined with HAXPES (with IMFP values lying well above 4 nm), enables drastically enhanced probing depth up to 30–70 nm depending on the X-ray excitation, and is suited for thick overlayers in 10 nm range, while being not adequate for ultra-thin layers. Rather, the latter would be best analyzed by XPS-IBA, where IMFPs are typically in the order of below 1 nm and up to 3 nm. Whether XPS or HAXPES should be chosen when performing IBA also depends on nature of the samples being analyzed: using XPS is not adequate for the samples generating partially overlapped photoelectron peaks, and in this case working from HAXPES spectra offers accessible, well separated high energy transitions suitable for background shape analysis.

For the best illustration on how IBA works, we present an example of HAXPES-IBA in Fig. 2, which depicts background analysis performed in QUASES-Analyze for Hf 3d in a pure, 3 mm HfO_2 sample. The inelastic background (red line) is subtracted from the measured spectrum (J(E), black line), leaving the no-loss spectrum (F(E), blue line). The inelastic background modeled for the depth distribution of the element is obtained by varying step by step, in the software, the thickness and buried depth of the layer from which the photoelectron originates, until a good match between J(E) and the modeled background is reached over the widest possible kinetic energy range. The result is appreciated by visual inspection of the spectra, in which the closeness of the fit between the simulated and measured background is evaluated in the kinetic energy range 30–100 eV after the peak (Fig. 2(a)). The exact peak shape in the energy region close to the peak energy up to ~10–20 eV below the peak energy is not accounted for by the model since it is largely determined by the chemical bond, lifetime broadening, and intrinsic excitations in the photoemission process which all may depend on the local chemical environment. Fig. 2(b) demonstrates a poor fit where the modeled HfO_2 distribution of 5–10 nm is incorrect. The simulated inelastic background is poorly-fitted to the measured background, and the subsequent no-loss spectrum does not lie at zero.

There are few parameters required from the user, since the principle source of information is the background shape. An effective inelastic mean free path ($IMFP_{eff}$) is calculated as the weighted average over the individual IMFP for each layer determined by the TPP-2M formula [30]. The weighted contribution is taken based on the thickness of each layer within the path the photoelectron travels out of the material, with a half-contribution from the layer from which the photoelectron originates. The half-contribution accounts for the probability of the photoelectron to originate at any depth within the layer and the choice of $IMFP_{eff1/2}$ for materials with similar inelastic scattering cross-sections has been extensively published upon [24,25,31]. A weighted IMFP ensures that the relatively high photoelectron transport in Al_2O_3 versus HfO_2 was accounted for in the inelastic background analysis.

The second parameter required by the software is the differential energy loss cross-section *K(E,T)*. *K(E,T)* is the probability for an electron of energy E to lose energy T per unit energy loss and path length traveled, and is essentially a delineation of the background after the no-loss peak. A universal cross-section of two mathematical parameters is available which accurately describes the background for most transition

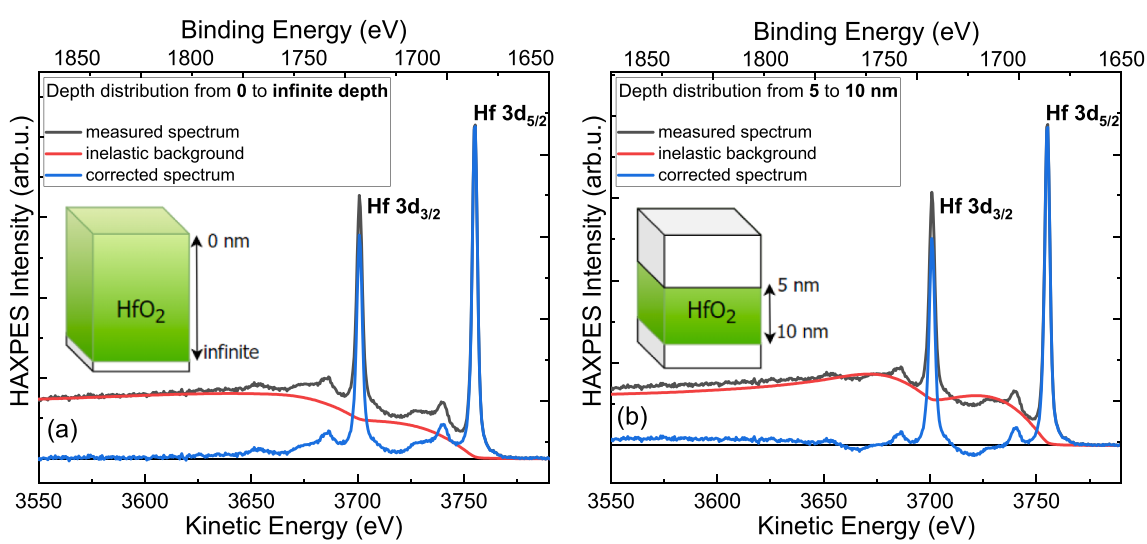

Fig. 2. QUASES-Analyze IBA of Hf 3d in bulk HfO_2 recorded with Cr Kα source. The black line is the raw measured data, and the red line is the inelastic background calculated by the software. The blue line is the spectrum which has been corrected for inelastic losses by subtracting the red line. A good fit between measured and calculated inelastic backgrounds is seen in (a) where the depth distribution of an infinite medium is accurate. A poor fit is seen in (b) where the depth distribution of 5–10 nm is incorrect. (For interpretation of the references to colour in this figure legend, the reader is referred to the web version of this article.)

metals and their alloys and oxides [32]. The equation is as follows:

$$\lambda(E)K(E,T) = \frac{BT}{(C+T^2)^2} \tag{8}$$

$B \cong 3000$ eV^2 and $C = 1643$ eV^2. B is normalized to $2C$, while C was determined via a dielectric-response calculation.

3. Results

3.1. Ultrathin Al_2O_3 layers

Tracking the ALD process in its early stages is important for both metrology and sample, but presents a challenge when following the increasing thickness of the layer. Highly accurate physical characterization techniques could nevertheless result in high error for an ultrathin deposition of only several angstroms. Chemical analyses determining the dose of an element in the material are accurate and precise, but at the cost of destroying the sample. In this section, we discuss the first class of ALD samples (Fig. 1(a)). In the study of ultrathin Al_2O_3 with a native silicon oxide layer, we first confirm the sensitivity and accuracy of nondestructive WDXRF against the destructive reference technique LPD-ICPMS in determining the Al dose. Now validated, WDXRF serves to confirm the pARXPS technique for thickness determinations in Al_2O_3 depositions with and without a HF-based surface preparation. The resulting pARXPS analyses demonstrate the method's ability to resolve the thickness of not only a layer of carbon contamination, but also the thickness of the buried SiO_2 layer present in the sample with an untreated surface.

3.1.1. LPD-ICPMS and WDXRF

In Fig. 3, we present the quantitative dose of Al in an Al_2O_3 ALD deposition process as determined by LPD-ICPMS and WDXRF. LPD-ICPMS was used as a destructive, whole surface and reference technique as it is calibrated with certified standards and has an estimated uncertainty of 10 % for the Al dose. The nondestructive WDXRF technique is confirmed by agreement with LPD-ICPMS to provide a quantitative determination of the dose of Al in an Al_2O_3 ALD deposition process with good uncertainty. Al surface concentration was measured in atoms per cm^2 of the sample. WDXRF layer thickness determination was converted to Al dose using the stoichiometric relationship between the thickness, density, and atomic weight of the material. The WDXRF values have a linear dependence and agreement within LPD-ICPMS uncertainties, with a scaling factor of 0.94 and a R^2 of 0.99. This confirms WDXRF as an appropriate reference technique for the following pARXPS methods.

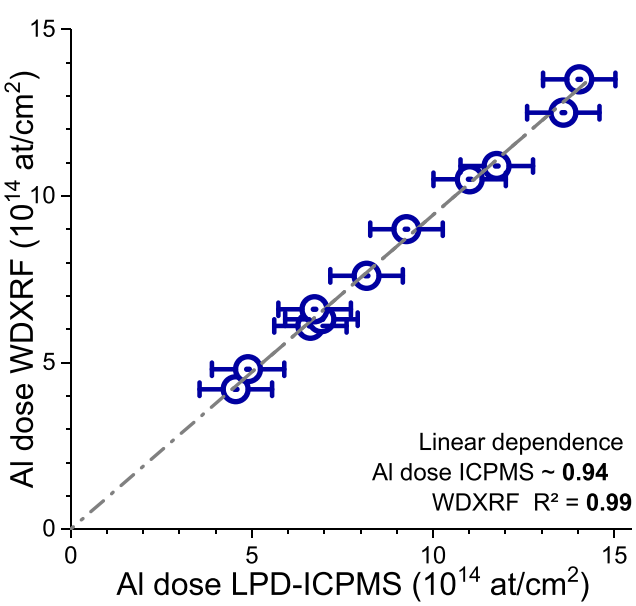

Fig. 3. Al Dose in ultrathin Al_2O_3 as determined by LPD-ICPMS and WDXRF. The experimental data (blue rings) demonstrate a linear dependence (gray dashed line). (For interpretation of the references to colour in this figure legend, the reader is referred to the web version of this article.)

3.1.2. pARXPS analysis

pARXPS was used as a non-destructive technique for the determination of the thicknesses of layers in an ALD process of ultrathin Al_2O_3 (ref. Fig. 1(a)) grown on SiO_2 with surface contamination in the form of adventitious carbon. Later, the same technique was used on ultrathin Al_2O_3 which was first treated with HF surface preparation which prevents the native oxide layer from forming. The principle of ARXPS is to consider the relationship between the intensity of the XPS signal as a function of angle and the depth distribution of the element in the material at the nm-scale. In pARXPS, spectra are collected over a wide angular range in parallel and without tilting the sample, permitting fast parallel acquisition and constant transmission. The experimental configuration permits analysis of every layer in the sample, including surface contamination and the oxide formed at the bulk-sample interface, which is impossible in solely chemical techniques (which would not discern the presence of the metal Si in two unique layers), nor solely physical techniques (which would be indiscriminate in layer ordering). Fig. 4 demonstrates the angular dependence of the Si-O signal from the native oxide layer and the Si-Si signal from the silicon substrate. The Si 2p spectrum has been normalized to the Si-O contribution, enabling a clear depiction of glancing angles producing very low intensity signals in the bulk contribution. The Al 2p peak which is attributed to the Al_2O_3 layer demonstrates the angular dependence of the core peak intensity.

The angular data in Fig. 4 can be accurately described by a 3-layer model with sharp interfaces as demonstrated in Fig. 5, where the pARXPS simulation data (dashed line) corresponds well to the intensity ratios determined experimentally (symbols). This agreement tends to confirm that interdiffusion is negligible in the stack. The sharp interfaces model relies on the contrast between two materials at the interface, and is specific to the ordering and position of the multilayer stack [33,34].

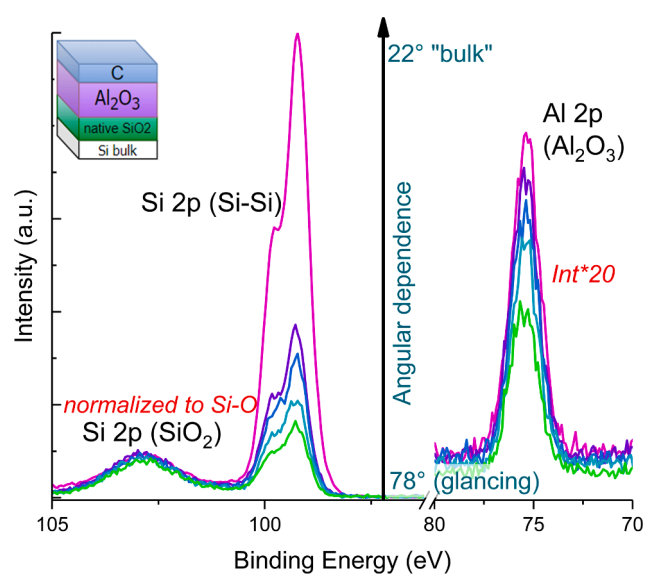

Fig. 4. pARXPS data of an ultrathin Al_2O_3 sample with carbon contamination for Si 2p (left panel) and Al 2p (right panel). The violet line is from spectra recorded at the glancing emission angle, while the green and blue are spectra recorded from smaller angles which probe the bulk of the sample. The Al 2p spectrum has been increased by a factor of 20 for visual purposes. (For interpretation of the references to colour in this figure legend, the reader is referred to the web version of this article.)

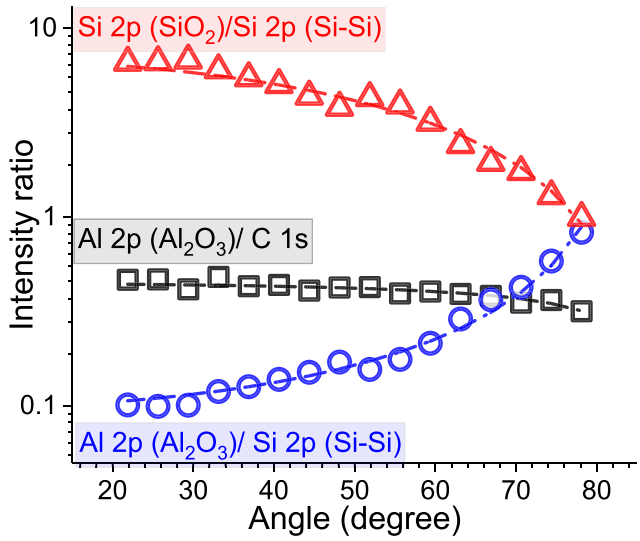

Fig. 5. Non-destructive depth profile of the ultrathin Al_2O_3 sample with carbon contamination and native SiO_2 layer. The pARXPS simulation values (dotted line) correspond well to the experimental values of the intensity ratio (symbols).

In Fig. 6, the thickness of the Al_2O_3 layer as determined by WDXRF and pARXPS is tracked with increasing ALD cycle repetitions. The two methods are well-correlated in the case of a chemical SiO_2 surface condition, with a less than one-percent difference between pARXPS and WDXRF determination. The thickness determinations by WDXRF and pARXPS are still correlated in the case of HF surface preparation, but differ at the extremities where pARXPS analysis shows greater thicknesses in earlier cycles, while WDXRF demonstrates greater layer thickness starting from 5 ALD cycles. The following section will discuss the linear growth mechanism of ALD, which explains the increased dependence of the chemical SiO_2 sample thicknesses in earlier cycles relative to those of the HF-prepared sample. These samples already have an established layer, so the ALD process reaches linear growth faster than the sample with only the substrate.

WDXRF, while non-destructive, is indiscriminate to the layer stacking order and position of the individual element. It is a physical analysis that provides the thickness of the layer without distinguishing between the silicon content in the bulk and its presence in the native oxide layer formed at the beginning of the deposition process. pARXPS allows the discrimination between the buried SiO_2 layer and the Si bulk. This permits unique characterizations for depositions with a HF prepared surface, where the SiO_2 layer is negligible, and unprepared surfaces, where the buried layer is distinguishable by the technique. ARXPS deduced the thickness of the approximately 0.8 nm layer of buried SiO_2 in the unprepared sample; as well as the $\leq$0.3 nm buried SiO_2 layer in the HF prepared sample.

In Fig. 7, pARXPS is confirmed to be effective in following the growth of ALD cycles from the starting phases up through the linear growth period. The pARXPS technique evidences the nucleation delay induced by HF surface preparation, followed by the expected linear growth once the surface is covered with Al_2O_3.

3.2. $SiO_2/HfO_2/Al_2O_3$ sample

Increasing complexity in a sample stack and thus the number of free parameters seldom improves the precision and accuracy of the characterization technique. In the following section, an ALD bilayer stack with layer thicknesses within the 1–2 nm range as shown in Fig. 1(b) is presented as an "intermediate" case for which several depth profiling techniques can be applied. We present IBA as a fast and accurate depth profiling alternative to the well-established XRR and pARXPS techniques. This sample appears in a previous work by Hönicke [10] in which it is evaluated with a reference-free GIXRF technique for quantifying the mass deposition of each layer. Hönicke's work demonstrates that the XRR technique suffers from uncertainties when dealing with ultrathin multilayered stacks. XRF at grazing incidence led to improved uncertainty in the mass deposition that is guaranteed by PTB National Metrology Institute and can be used to assess IBA and pARXPS [10]. First we discuss the result from the GIXRF reference technique in determining the mass deposition of Hf and Al in the sample as compared to determinations through the sharp-interfaces model of ARXPS [35]. In order to compare the quantifications, the thickness obtained from ARXPS analysis (nm) is related to the density of the material (g/cc), delivering the mass deposition (ng/mm^2) of each element in the sample. GIXRF gives a value of 3.14 $\pm$ 0.24 ng/mm^2 for the mass deposition of Al, while the ARXPS calculation yields 2.90 ng/mm^2. Hf mass deposition is 7.4 $\pm$ 0.6 ng/mm^2 according to GIXRF, and 9.0 ng/mm^2 by ARXPS. The proximity in these values further supports ARXPS as a quantitative method for depth profiling in high-*k* ALD samples.

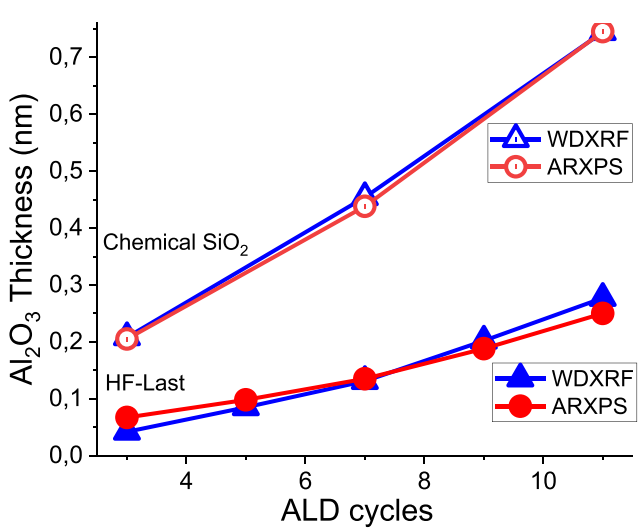

Fig. 6. Al_2O_3 thickness as a function of the number of ALD cycles for chemical SiO_2 and HF-last sample preparation as determined by pARXPS (circles) and WDXRF (triangles).

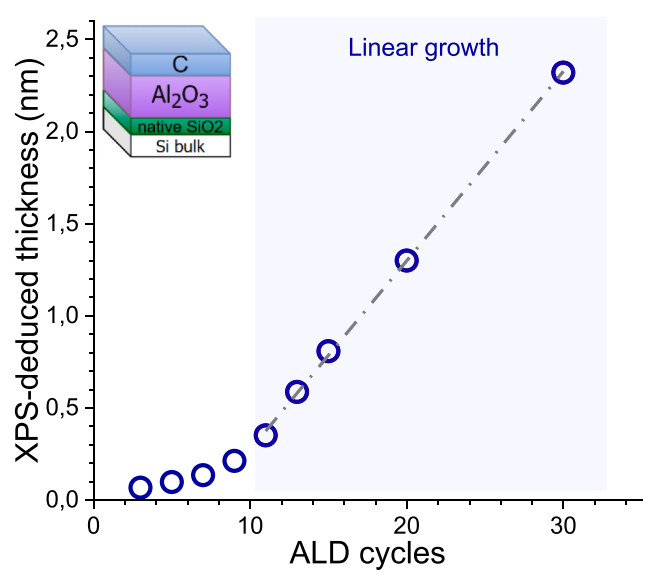

Fig. 7. pARXPS thickness determinations as a function of ALD cycle for an ultrathin Al_2O_3 sample with a HF-last surface preparation. Linear growth (gray dashed line) is seen after approximately 12 cycles.

The bilayer sample was subjected to additional analyses by IBA of the Al Kα XPS spectrum. Here, IBA is proposed as a fast and non-destructive depth profiling method which, unlike ARXPS, is sensitive several nanometers deep into the material. In contrast to ARXPS, which requires high-resolution core-level spectra of each element for several angles, IBA utilizes a single survey scan from which to extract depth distribution information. For metrological purposes it is desirable to implement IBA with an optimal accuracy and ease of implementation enabled by spectrum analysis with minimal signal noise. Here, we investigate how gentle surface in-situ cleaning can improve the IBA analysis.

Fig. 8 presents a complete depth profiling by IBA of a bilayer SiO_2/HfO_2/Al_2O_3 stack. The analysis was done before and after surface treatment using Gas Cluster Ion Beams (GCIB) for removing adventitious carbon contamination. The depth distribution of oxygen is taken to represent the overall thickness of the stack comprised of HfO_2, Al_2O_3, and SiO_2. The depth distribution of Hf, from Hf $4p_{3/2}$ IBA, can then be taken to indicate the HfO_2 layer, the subtraction of which enables inferring Al_2O_3 and SiO_2 overall thickness. Al 2p peak lies in the low binding energy region where peak overlap with Si 2p and Si 2s prevent IBA for either species. Indeed, IBA requires that the background spectra be approximately 100 eV long and free of peaks from other elements. This is in order to prevent interference in the background signal. The results are compared with thickness determinations by ARXPS and GIXRF for which the mass deposition has been converted to thickness by using the nominal densities of AlO_2 and HfO_2.

Fig. 8(a) and (c) reflect large and well-defined Hf 4p and O 1s peaks with pronounced backgrounds indicative of a wide elemental distribution in the sample. The resulting depth distribution for oxygen is from the surface of the material to 6.3 nm deep. The fit remains constant along the kinetic energy range. Concerning the Hf, the "bump" in the spectrum at 1050 eV is the Hf $4p_{1/2}$ peak, and is not included in evaluation of the fit since it originates from the same element. A resulting depth distribution of 3.0–5.5 nm for a thickness of 2.5 nm is not aligned with the expected 1.5 nm thickness of HfO_2 in the sample nor the modeled depth distribution of oxygen minus 1 nm SiO_2 and 2 nm of Al_2O_3. The start depth of 3.0 nm is also not consistent with the anticipated 2 nm thickness of the Al_2O_3 overlayer. A significant photoelectron signal from C 1s was evident in the spectra, and could suggest a layer of surface contamination.

After surface treatment by argon, the signal noise in both spectra is somewhat diminished. The resulting depth distribution of oxygen is from 0.5 nm below the surface to 4.5 nm deep. The carbon signal was

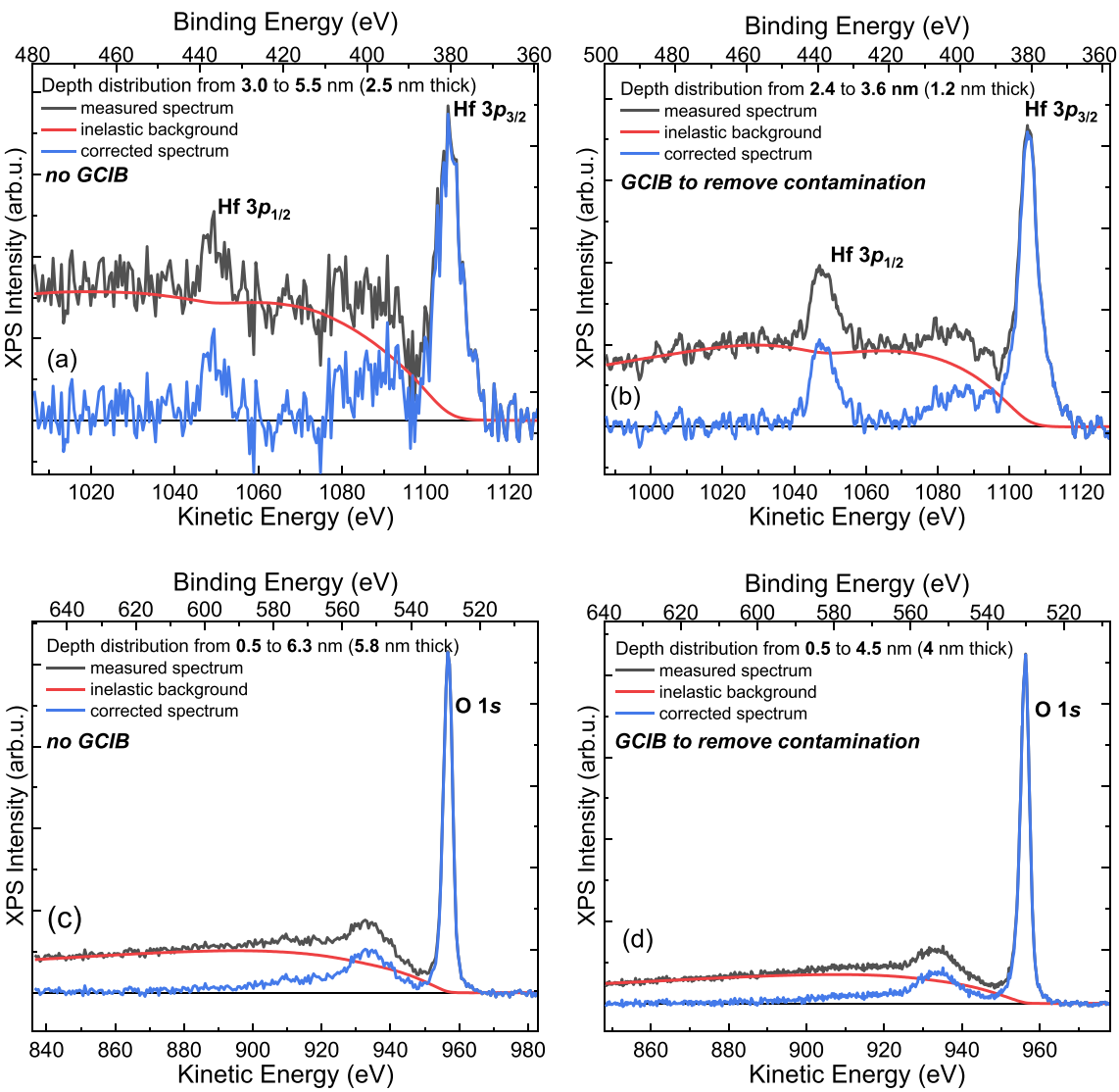

Fig. 8. QUASES-Analyze IBA for the ALD bilayer stack: HfO_2 (1.5 nm) buried under Al_2O_3 (2 nm) before and after GCIB treatment. The black line is the raw measured spectrum, the red line is the calculated inelastic background, and the blue line is the spectrum corrected for inelastic losses by subtracting the red line. (For interpretation of the references to colour in this figure legend, the reader is referred to the web version of this article.)

eliminated after surface treatment, so the displacement of O 1s is unlikely to be from contamination. Rather, the oxygen content is different across the three metal oxide layers, and so the photoelectron transport is unlikely to be perfectly reproducible. While elastic effects are not considered in the software modeling, they do have a minute influence on the transport process which could come into play for this error in the analysis. In Fig. 7(d), the fit between the modeled and experimental background has improved, and the resolution increased significantly. In alignment with oxygen modeling after removal of surface contamination, hafnium is shown modeled at a depth from 2.4 to 3.6 nm. Thus the XPS-IBA results are well-aligned to the nominal values administered in the ALD process.

Fig. 9 shows that IBA with GCIB is accurate to nominal deposition data within 6 % and provides information on the location of interfaces within a tenth of a nanometer. In addition to being a faster method than pARXPS, less information on the sample is needed for IBA. pARXPS can provide a more precise measurement, with a precision down to a tenth of an angstrom. As material layers get too thick for pARXPS, IBA becomes the more relevant depth profiling technique for depth profiling. This is demonstrated in the following section.

3.3. Buried layer HfO_2/Al_2O_3 samples

In some technologies such as power nanoelectronics, a larger thickness of the dielectric layers is required compared to logic applications, in a range where traditional XPS techniques are limited by the IMFP of the element, itself directly related to the energy of the X-ray source. It is therefore necessary to investigate lab-based analytical methods for determining depth distributions within some tens of nm below the surface. ARXPS especially is relegated to a purely surface-sensitive technique, for which the typically 1 nm-IMFP does not allow probing more than 10 nm. For truly buried layers lying under a top electrode, capping layer, or dielectric, a higher energy source is necessary for non-destructive depth profiling of the critical interfaces. Lab-based HAXPES using a Cr Kα source was evaluated on six samples of Al_2O_3 and HfO_2 stacks with increasingly thick overlayers (Fig. 1(c)). The layers were thick enough to use XRR technique as a reference to assess IBA results.

3.3.1. HAXPES survey spectrum

Fig. 10 presents the HAXPES scans acquired for the sample containing an approximately 9.2 nm-thick Al_2O_3 overlayer and 2.7 nm-thick buried HfO_2 layer. The right side of the spectrum depicts the low binding energy signals (i.e. high kinetic energy region) which are accessible through traditional XPS, and where overlapping peaks and background signals make IBA not applicable.

In the low kinetic energy region (i.e. high binding energy), the deeper Si 1s, Hf 3*d*, and Al 1s core levels are well suited for analysis because of no peak overlap, unlike the XPS case. These transitions are necessary for a complete depth profiling of the samples incorporating each element present in the material.

Fig. 11 depicts the inelastic background analysis performed in QUASES-Analyze for the four elements making up sample A1 in the

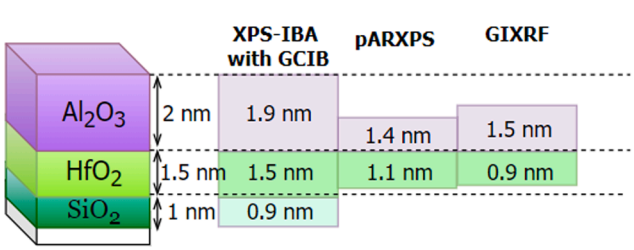

Fig. 9. Comparison of thickness determinations by IBA, pARXPS, and GIXRF. IBA distributions are shown for before and after a GCIB surface treatment in order to remove contamination.

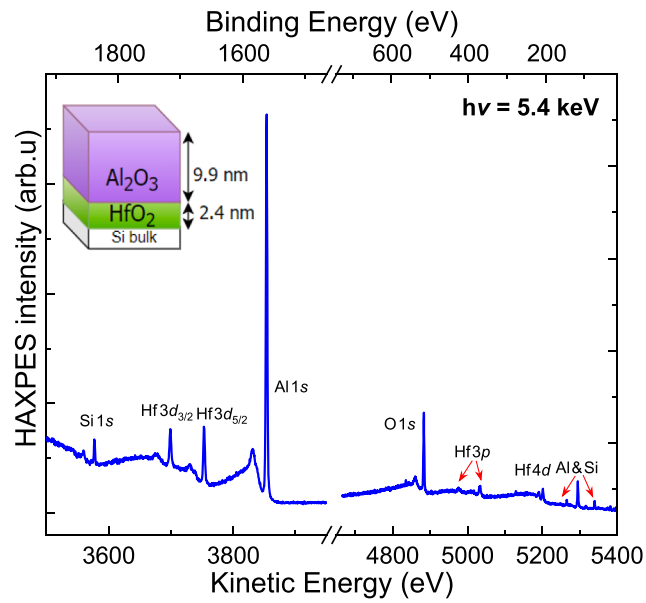

Fig. 10. Cr Kα HAXPES spectrum of buried HfO_2 with Al_2O_3 overlayer. The left side of the spectrum contains high energy transitions which are not available with an Al Kα X-ray source.

series. A1 has an Al_2O_3 overlayer with a thickness of 9.9 nm, with a 2.4 nm thick HfO_2 layer buried beneath. The best match scenario in the inelastic background analysis is evaluated by visual inspection between the modeled and measured backgrounds. Precision in the range of start and end depths corresponding to an acceptable match is increased by cross-correlating the depth distributions of all elements making up the bilayer sample. Through this method a unique solution is achieved which is independent of other analyses. The modeled Al 1s background shape corresponds to the best match obtained for an Al depth distribution between 0.5 and 10.4 nm below the surface: this is in excellent agreement with the thickness measurement obtained by XRR, which determines a thickness of 9.9 nm for the alumina layer. The shifted start depth of the Al 1s layer is most likely due to surface contamination of the overlayer, since no pre-cleaning was performed prior the measurements. The universal inelastic scattering cross-section used in this analysis does not account for the chemical-state dependent features close to the no-loss peak, nor does it account for plasmon features. It is for this reason that the calculated background does not account for the region 30 eV after the peak for any of the elements. The modeled inelastic background of Hf 3d nearly takes into account the background between the two peaks, with the closest relation between the calculated and measure background corresponding to a start depth of 12.2 nm and end depth of 14.6 nm. Therefore, the nominal thickness of the hafnia layer is accurate and able to be analyzed through HAXPES-IBA. The Si 1s spectrum contains a significant inelastic background whose intensity exceeds the no-loss peak. This is consistent for a deeply buried element whose photoelectron will undergo many inelastic loss collisions during transport. The total thickness of the Al 1s and Hf 3d distributions is 12.3 nm. The IBA fit for O 1s, however, is best represented by a depth distribution of 0.3 to 13.9 nm for a total thickness of 13.6 nm.. It should be noted that the interface of the oxide and the Si substrate is likely not two discrete layers, as a chemical oxide is likely to have formed. The wider depth distribution of O 1s may support this, and the uncertainty in the IBA of the deeply buried Si 1s would permit the presence of such an oxide layer. Unfortunately, the thickness of these samples coupled with the uncertainty of the IBA for oxygen does not permit this method to characterize such a feature.

Complete depth profiling was achieved for six samples, named in this work A1, A2, A3, H1, H2, and H3 (see Table 1). The analysis of every element in the sample permitted the cross-confirmation of interface

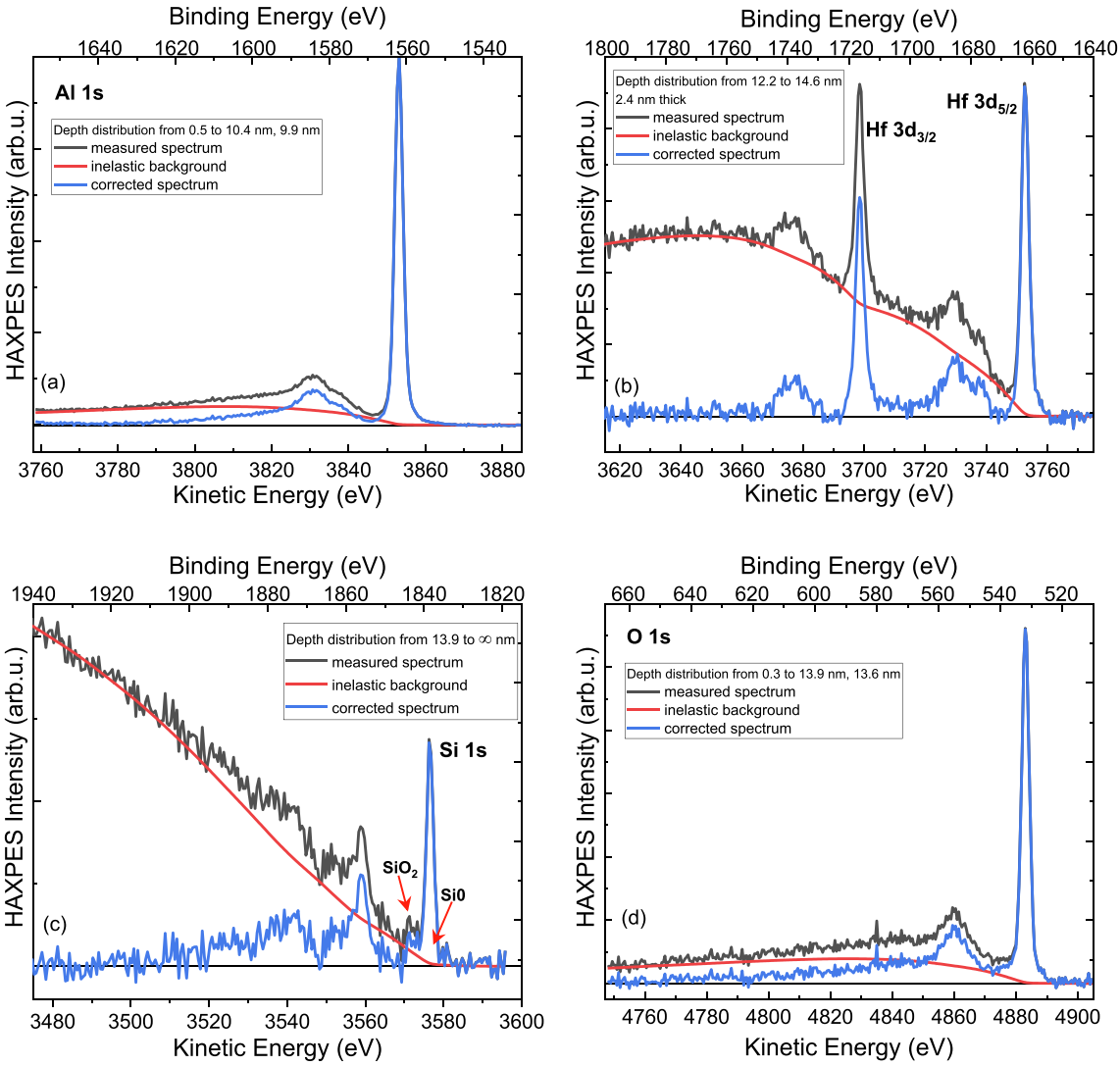

Fig. 11. QUASES-Analyze IBA for sample A1: HfO_2 (2.4 nm) buried under Al_2O_3 (9.9 nm). The elemental distributions for the Al 1s and Hf 3d peaks support anticipated thickness of the sample. Si 1s and O 1s suggest a thicker sample, with possibly an oxidized layer of contamination. A SiO_2 component may be visible in the Si 1s spectrum.

positions and layer thicknesses. The uncertainty of the analysis is determined from the smallest depth increment which does not significantly change the quality of the fit. In our study it is between 1 and 4 Å in the start depth, 4 Å to 1 nm in the interface between the oxides, and 3–5 Å in the bottom interface with Si. In the spectra of the HfO_2 overlayer samples, the continuous background before the O 1s signal was blocked by preceding Hf signals and the overlapping Hf 4 s signal, preventing its analysis. This obstacle was circumvented by accessing the O KLL peak at 4.9 keV and using a smaller emission angle. Table 1 depicts the thickness determinations and interface positions of each layer in the six samples, and the results are compared to XRR measurements. The uncertainty value is determined based on the range of possible start and end depths which generate a calculated inelastic background that is visually appraised to be in alignment with that of the experimental spectrum over the largest possible energy range excluding the first plasmon. Confirmation of layer thickness is derived from the start and end depth of individual core signals from Al 1s, Hf $3d_{5/2}$, and Si 1s. Information on the location of the interface comes from the relative start and end depth of the buried layer and overlayer, respectively. The difference between the start depth the overlayer and the start depth of the Si substrate can be interpreted as the overall thickness, as can the distribution of O 1s, which is present throughout the sample. These reference points can be compared with the background analysis for the less-precise buried layer boundaries. O 1s is generally less-precise and accurate, likely due to changing oxygen content in the two oxides. O KLL has an IMFP several nanometers shorter than the other species, and as such provides less in-depth information. For this reason, only the metal element IBA is discussed in the table.

3.3.2. *Al_2O_3 overlayer samples A1, A2, A3*

As shown in Table 1, Al 1s distribution in the A1 overlayer is very precise, with the start and end depths corresponding to a good agreement between the calculated and measured backgrounds whose closeness of fit varied only 0.1 nm in either direction. The Hf 3d signal from the 2.4 nm buried HfO_2 layer does not demonstrate the anticipated spatial depth distribution, but does present a median thickness in line with XRR measurements. The optimal start and end depth in relation to the simulated background as fitted to the measured reflects a two-nanometer shift deeper into the bulk and away from the Al 1s interface. This also pushes the modeled layer two nanometers into the Si 1s distribution. This is notable because it confirms that the relative start depths of Al 1s and Si 1s are in agreement amongst themselves and with the XRR results, eviting the necessity of oxygen and acounting for inaccuracy in the Hf $3d_{5/2}$ IBA. In this sample stack, the relative

Table 1
Comparison of the results from XRR and inelastic background analyses on every sample. Numbers in bold indicate the location of the interface. IBA results were derived from agreement between Al 1s, Hf $3d_{5/2}$, Si 1s.

Sample	Layer	XRR thickness (nm)	IBA thickness (nm)	IBA depth distribution (nm)
A1	Al_2O_3	9.9	9.9 ± 0.2	0.5 ± 0.1 to **10.4** ± 0.1
	HfO_2	2.4	2.4 ± 1.1	**12.2** ± 0.5 to **14.6** ± 0.6
	Surface to Si	12.3	12.4 ± 0.6	**12.9** ± 0.5
A2	Al_2O_3	14.8	14.8 ± 0.2	0.3 ± 0.1 to **15.1** ± 0.1
	HfO_2	2.4	2.4 ± 0.9	**15.7** ± 0.4 to **18.1** ± 0.5
	Surface to Si	17.2	17.2 ± 0.4	**17.5** ± 0.3
A3	Al_2O_3	24.4	24.4 ± 0.5	0 ± 0.1 to **24.4** ± 0.4
	HfO_2	2.4	2.4 ± 1.8	**24.4** ± 0.8 to **26.8** ± 1
	Surface to Si	26.8	26.8 ± 0.6	**26.8** ± 0.5
H1	HfO_2	9.2	9.2 ± 0.2	0.1 ± 0.1 to **9.3** ± 0.1
	Al_2O_3	2.7	2.8 ± 1	**9.2** ± 0.5 to **12** ± 0.5
	Surface to Si	11.9	11.9 ± 0.6	**12** ± 0.5
H2	HfO_2	13.6	13.6 ± 0.8	**0.4** ± 0.4 to **14** ± 0.4
	Al_2O_3	2.8	2.8 ± 1	**14.6** ± 0.5 to **17.4** ± 0.5
	Surface to Si	16.4	17.1 ± 0.8	**17.5** ± 0.8
H3	HfO_2	18.2	18.2 ± 0.9	0.5 ± 0.4 to 18.7 ± 0.4
	Al_2O_3	2.8	–	–
	Surface to Si	21	21 ± 1	21.5 ± 1

thicknesses of the overlayer and buried layer are close. HfO_2 is denser than Al_2O_3, and the Al 1s is within 100 eV of the Hf $3d_{5/2}$ signal. For this reason, the IBA for Hf $3d_{5/2}$ cannot accurately discern the impact of the inelastic background in this region. The buried HfO_2 layer in A2 is similarly shifted as in A1, but less pronounced. Again, the Si 1s and Al 1s distributions agree in the anticipated interface positions, and the buried layer thickness is in accordance with XRR determinations and the Hf $3d_{5/2}$ background analysis. In the sample with the thickest Al_2O_3 overlayer, A3, the median interface determinations are common amongst all background analyses. The precision in the boundary positions, however, is the lowest amongst all of the samples. This is expected, as less information is available at greater depths, and there is a greater possibility of scattering events which do not make up the calculated inelastic background.

In the spectra for the samples comprised of a HfO_2 overlayer and buried Al_2O_3, the Hf 4 s signal at 4877 eV kinetic energy strongly eclipses the O 1s signal at 4884 eV. As mentioned in the previous section, this prevents the inelastic background analysis of O 1s, necessitating the inclusion of the O KLL Auger signal at 508 eV KE. Lying at such a low kinetic energy, O KLL Auger electron has an IMFP several nanometers shorter than the other core lines used for depth profiling. As a result, the inelastic background analysis for O KLL is not reliable as an independent indicator of depth distribution, but was used to confirm the analyses for the Al 1s, Hf $3d_{5/2}$, and Si 1s signals.

3.3.3. *HfO_2 overlayer samples H1, H2, H3*

In H1, the median end depth of Al 1s and start depth of Hf $3d_{5/2}$ support the position of the interface as lying 9.3–9.2 nm below the surface. The Al_2O_3-Si substrate interface is similarly precise as the median Al 1s distribution ends at the exact point of the Si 1s start depth. The inelastic background analysis for each element in H2 reflects an offset of the oxide materials from the surface of the sample, although at varying degrees of impact. Carbon was evident in the spectra of each sample, suggesting surface contamination which could have impacted the analysis. The resulting overall thickness deviated 0.6 nm from the nominal thickness. Despite the implementation of an increased takeoff angle, the Al 1s signal could not be meaningfully resolved in H3 in order to facilitate analysis of the inelastic background. This is due in part to the weak signal of Al 1s as it travels through the dense HfO_2 layer, but also as a result of the especially strong Hf $3d_{5/2}$ signal which follows just 100 eV behind. The thickness of Al 1s is therefore determined by the relative end depth of Hf $3d_{5/2}$ and start depth of Si 1s. Sensitivity of the technique is lower in the HfO_2 overlayer series due to the density of HfO_2 and its contribution to the reduced inelastic mean free path of the buried species. Further experiments increasing the takeoff angle of the experiment did not improve resolution of Al 1s in H3.

4. Conclusion

This work was performed in the technological context of stronger requirements for non-destructive characterization and metrology of ALD dielectric oxide layer stacks with increasing material thicknesses in the 1–30 nm range, for applications from logic to power transistor devices. We have presented highly-calibrated, destructive metrology techniques as references, and assessed the implementation of alternative, non-destructive X-ray photoelectron spectroscopic methods. In the study of ultrathin ($\leq$2 nm) Al_2O_3 layers a linear dependence between LPD-ICPMS and WDXRF dose determinations of the amount of aluminum in a sample confirmed WDXRF to be a quantitative and precise technique. Thickness measurements using pARXPS and IBA-XPS were compared to the latter reference technique. IBA-XPS combined with GCIB cleaning before the measurement was shown to greatly improve the layer thickness determinations with less than a 10 % error from the nominal values. IBA-XPS also provided information on the 1 nm SiO_2 layer at the Si substrate interface. pARXPS, however, was more accurate to the GIXRF reference technique, and provides an additional decimal of precision. This is anticipated for ultrathin layers, where a technique capable of tracking minute changes in the data is necessary. For dielectric layer thicknesses in the 10–25 nm range and <3 nm-thick buried layers, Cr Kα-based lab-scale HAXPES combined with IBA was evaluated for the thickness determination and compared to an XRR metrology technique. The method afforded the analysis of each element in the oxide layers including oxygen by use of the O KLL Auger transition. Through this method, a complete depth profiling was achieved independent of a reference technique with resulting thickness values in excellent agreement with XRR for both the surface and buried layers. The thickness determination is accurate with an uncertainty below 6 % for the surface layer with an expected increased uncertainty in the buried layer. In summary, we explored the unique performance of XPS, which can reliably reveal depth-dependent elemental distributions in a wide range of sample thicknesses. From monolayers to layers tens of nanometers thick, pARXPS, HAXPES, and investigation of the inelastic background permitted non-destructive depth profiling with <50 nm spatial resolution. This aligns with industrial needs for inline process control by XPS analysis.

5. Perspectives

The XPS and HAXPES methods discussed in paper have several

potential applications. In thin samples, pARXPS can be applied in the study of chemical effects the thickness of the native oxide layer may have on the proceding structure. For more complete devices, HAXPES-IBA could permit the analysis of active multilayer structures buried beneath a top electrode or dielectric in a finished material. The methods discussed are applicable to other complementary metal-oxide semiconductor systems as well. For example, Ta_2O_5 and Si have been shown to experience an interfacial reaction which forms a thin SiO_x layer at the interface, and oxynitrides have been explored as barriers between the high-*k* metal oxides and Si substrate [4]. Both methods could provide information on these buried interfaces in differentiating between the native oxide and the substrate without disrupting the interfacial phenomena. The inelastic background analysis methods can approach a more quantitative assessment through error analysis of the fit between the simulated and measured background. This has been explored in previous work [23–27]. Future work can employ a bulk reference spectrum in the place of the universal inelastic scattering cross-section in order to simulate a background which is well-fitted to the measured inelastic background, and thus amenable to a statistical analysis.

CRediT authorship contribution statement

T.R. Bure: Investigation, Writing – original draft, Writing – review & editing. **O. Renault:** Supervision, Conceptualization, Methodology, Validation. **E. Nolot:** Supervision, Conceptualization, Methodology, Validation, Resources, Writing – original draft. **T. Lardin:** Conceptualization, Resources. **C. Robert-Goumet:** Supervision, Conceptualization. **N. Pauly:** Supervision, Conceptualization, Validation.

Declaration of Competing Interest

The authors declare that they have no known competing financial interests or personal relationships that could have appeared to influence the work reported in this paper.

Acknowledgments

(Part of) this work, carried out on the Platform for Nano-characterisation (PFNC), was supported by the "Recherches Technologiques de Base" program of the French National Research Agency (ANR)".

This work was supported by the French National Research Agency (ANR) under the "Investissements d'avenir" program ANR-10-EQPX-0033 (EQUIPEX IMPACT).

We thank financial support from Hubert Curien project Tournesol n°46254PL.

References

[1] J. Lutz, H. Schlangenotto, U. Scheuermann, R. De Doncker, Semiconductor Power Devices, Springer International Publishing, Cham, 2018 https://doi.org/10.1007/978-3-319-70917-8.
[2] J. Azadmanjiri, C.C. Berndt, J. Wang, A. Kapoor, V.K. Srivastava, C. Wen, A review on hybrid nanolaminate materials synthesized by deposition techniques for energy storage applications, J. Mater. Chem. A. 2 (2014) 3695–3708, https://doi.org/10.1039/C3TA14034B.
[3] T. Hori, Gate Dielectrics and MOS ULSIs: Principles, Technologies and Applications, Springer, Berlin Heidelberg, 1997 https://doi.org/10.1007/978-3-642-60856-8.
[4] G.D. Wilk, R.M. Wallace, J.M. Anthony, High-κ gate dielectrics: current status and materials properties considerations, J. Appl. Phys. 89 (2001) 5243–5275, https://doi.org/10.1063/1.1361065.
[5] P.K. Park, E.-S. Cha, S.-W. Kang, Interface effect on dielectric constant of HfO2/Al2O3 nanolaminate films deposited by plasma-enhanced atomic layer deposition, Appl. Phys. Lett. 90 (2007) 232906, https://doi.org/10.1063/1.2746416.
[6] G.N. Parsons, S.M. George, M. Knez, Progress and future directions for atomic layer deposition and ALD-based chemistry, MRS Bull. 36 (2011) 865–871, https://doi.org/10.1557/mrs.2011.238.
[7] S.M. George, Atomic layer deposition: an overview, Chem. Rev. 110 (2010) 111–131, https://doi.org/10.1021/cr900056b.
[8] S. Hüfner, Photoelectron Spectroscopy, Springer, Berlin Heidelberg, 2003 https://doi.org/10.1007/978-3-662-09280-4.
[9] P.Y. Hung, C. Gondran, A. Ghatak-Roy, S. Terada, B. Bunday, H. Yeung, A. Diebold, X-ray reflectometry and x-ray fluorescence monitoring of the atomic layer deposition process for high-k gate dielectrics, J. Vac. Sci. Technol. B. 23 (2005) 2244, https://doi.org/10.1116/1.2009774.
[10] P. Hönicke, B. Detlefs, E. Nolot, Y. Kayser, U. Mühle, B. Pollakowski, B. Beckhoff, Reference-free grazing incidence x-ray fluorescence and reflectometry as a methodology for independent validation of x-ray reflectometry on ultrathin layer stacks and a depth-dependent characterization, J. Vac. Sci. Technol. A. 37 (2019) 7, https://doi.org/10.1116/1.5094891.
[11] B.S. Semak, C. van der Marel, S. Tougaard, Comparison of the Tougaard, ARXPS, RBS and ellipsometry methods to determine the thickness of thin SiO2 layers, Surf. Int. Anal. 33 (2002) 238–244, https://doi.org/10.1002/sia.1206.
[12] P. Colombi, D.K. Agnihotri, V.E. Asadchikov, E. Bontempi, D.K. Bowen, C. H. Chang, L.E. Depero, M. Farnworth, T. Fujimoto, A. Gibaud, M. Jergel, M. Krumrey, T.A. Lafford, A. Lamperti, T. Ma, R.J. Matyi, M. Meduna, S. Milita, K. Sakurai, L. Shabel'nikov, A. Ulyanenkov, A. Van der Lee, C. Wiemer,, Reproducibility in X-ray reflectometry: results from the first world-wide round-robin experiment, J. Appl. Crystallogr. 41 (2008) 143–152, https://doi.org/10.1107/S0021889807051904.
[13] L. Fauquier, B. Pelissier, D. Jalabert, F. Pierre, R. Gassilloud, D. Doloy, C. Beitia, T. Baron, Depth profiling investigation by pARXPS and MEIS of advanced transistor technology gate stack, Microelectron. Eng. 169 (2017) 24–28, https://doi.org/10.1016/j.mee.2016.11.018.
[14] S. Tougaard, Background removal in x-ray photoelectron spectroscopy: relative importance of intrinsic and extrinsic processes, Phys. Rev. B. 34 (1986) 6779–6783, https://doi.org/10.1103/PhysRevB.34.6779.
[15] S. Tougaard, Practical guide to the use of backgrounds in quantitative XPS, J. Vac. Sci. Technol. A. 39 (2021) 011201, https://doi.org/10.1116/6.0000661.
[16] K. Watanabe, H. Yamazui, R. Inoue, New application fields developed by Hard X-ray Photoelectron Spectroscopy: "PHI Quantes," (n.d.) 8.
[17] M. Kobata, I. Píš, H. Iwai, H. Yamazui, H. Takahashi, M. Suzuki, H. Matsuda, H. Daimon, K. Kobayashi, Development of the hard-X-ray angle resolved X-ray photoemission spectrometer for laboratory use, Anal. Sci. 26 (2010) 227–232, https://doi.org/10.2116/analsci.26.227.
[18] W. Fredriksson, S. Malmgren, T. Gustafsson, M. Gorgoi, K. Edström, Full depth profile of passive films on 316L stainless steel based on high resolution HAXPES in combination with ARXPS, Appl. Surf. Sci. 258 (2012) 5790–5797, https://doi.org/10.1016/j.apsusc.2012.02.099.
[19] J.F. Watts, J. Wolstenholme, An Introduction to Surface Analysis by XPS and AES, second ed., Wiley, Hoboken, 2019.
[20] E. Nolot, S. Cadot, F. Martin, P. Hoenicke, C. Zech, B. Beckhoff, In-line characterization of ultrathin transition metal dichalcogenides using X-ray fluorescence and X-ray photoelectron spectroscopy, Spectrochim. Acta Part B At. Spectrosc. 166 (2020), https://doi.org/10.1016/j.sab.2020.105788.
[21] S. Tougaard, Software Packages to Characterize Surface Nano-Structures by Analysis of Electron Spectra, 2021. <http://www.quases.com/>.
[22] S. Tougaard, Energy loss in XPS: Fundamental processes and applications for quantification, non-destructive depth profiling and 3D imaging, J. Electron Spectrosc. Relat. Phenom. 178–179 (2010) 128–153, https://doi.org/10.1016/j.elspec.2009.08.005.
[23] P. Risterucci, O. Renault, C. Zborowski, D. Bertrand, A. Torres, J.-P. Rueff, D. Ceolin, G. Grenet, S. Tougaard, Effective inelastic scattering cross-sections for background analysis in HAXPES of deeply buried layers, Appl. Surf. Sci. 402 (2017) 78–85, https://doi.org/10.1016/j.apsusc.2017.01.046.
[24] C. Zborowski, O. Renault, A. Torres, Y. Yamashita, G. Grenet, S. Tougaard, Determination of the input parameters for inelastic background analysis combined with HAXPES using a reference sample, Appl. Surf. Sci. 432 (2018) 60–70, https://doi.org/10.1016/j.apsusc.2017.06.081.
[25] C. Zborowski, O. Renault, A. Torres, C. Guedj, Y. Yamashita, S. Ueda, G. Grenet, S. Tougaard, Quantitative determination of elemental diffusion from deeply buried layers by photoelectron spectroscopy, J. Appl. Phys. 124 (2018) 085115, https://doi.org/10.1063/1.5033453.
[26] P. Risterucci, O. Renault, E. Martinez, B. Detlefs, V. Delaye, J. Zegenhagen, C. Gaumer, G. Grenet, S. Tougaard, Probing deeper by hard x-ray photoelectron spectroscopy, Appl. Phys. Lett. 104 (2014) 051608, https://doi.org/10.1063/1.4864488.
[27] P. Risterucci, O. Renault, E. Martinez, B. Detlefs, J. Zegenhagen, G. Grenet, S. Tougaard, Inelastic background analysis of HAXPES spectra: towards enhanced bulk sensitivity in photoemission: Inelastic background analysis of HAXPES spectra, Surf. Interface Anal. 46 (2014) 906–910, https://doi.org/10.1002/sia.5484.
[28] B.F. Spencer, S. Maniyarasu, B.P. Reed, D.J.H. Cant, R. Ahumada-Lazo, A. G. Thomas, C.A. Muryn, M. Maschek, S.K. Eriksson, T. Wiell, T.-L. Lee, S. Tougaard, A.G. Shard, W.R. Flavell, Inelastic background modelling applied to hard X-ray photoelectron spectroscopy of deeply buried layers: a comparison of synchrotron and lab-based (9.25 keV) measurements, Appl. Surf. Sci. 541 (2021) 148635, https://doi.org/10.1016/j.apsusc.2020.148635.
[29] S. Tougaard, Accuracy of the non-destructive surface nanostructure quantification technique based on analysis of the XPS or AES peak shape, Surf. Interface Anal. 26 (1998) 249–269, https://doi.org/10.1002/(SICI)1096-9918(199804)26:4<249::AID-SIA368>3.0.CO;2-A.
[30] S. Tanuma, C.J. Powell, D.R. Penn, Calculation of electron inelastic mean free paths (IMFPs) VII. Reliability of the TPP-2M IMFP predictive equation, Surf. Interface Anal. 35 (2003) 268–275, https://doi.org/10.1002/sia.1526.

[31] C. Zborowski, S. Tougaard, Theoretical study toward rationalizing inelastic background analysis of buried layers in XPS and HAXPES, Surf. Interface Anal. 51 (2019) 857–873, https://doi.org/10.1002/sia.6660.
[32] S. Tougaard, Universality classes of inelastic electron scattering cross-sections, Surf. Interface Anal. 25 (1997) 137–154, https://doi.org/10.1002/(SICI)1096-9918(199703)25:3<137::AID-SIA230>3.0.CO;2-L.
[33] A.K. Livesey, G.C. Smith, The determination of depth profiles from angle-dependent XPS using maximum entropy data analysis, J. Electron Spectrosc. Relat. Phenom. 67 (1994) 439–461, https://doi.org/10.1016/0368-2048(93)02035-K.
[34] M.A. Scorciapino, G. Navarra, B. Elsener, A. Rossi, Nondestructive surface depth profiles from angle-resolved x-ray photoelectron spectroscopy data using the maximum entropy method. I. A new protocol, J. Phys. Chem. C. 113 (2009) 21328–21337, https://doi.org/10.1021/jp906326m.
[35] B.J. Tielsch, J.E. Fulghum, Application of angle-resolved XPS algorithms to overlayers and concentration gradients, Surf. Interface Anal. 21 (1994) 621–630, https://doi.org/10.1002/sia.740210905.

Glossary

ALD: Atomic Layer Deposition
WDXRF: Wavelength Dispersive X-ray Fluorescence
LPD-ICPMS: Liquid-Phase Deposition Inductively Coupled Plasma Mass Spectrometry
Parxps: Parallel Angle Resolved X-ray Photoelectron Spectroscopy
GIXRF: Grazing Incidence X-ray Fluorescence
IBA: Inelastic Background Analysis
HAXPES: Hard X-ray Photoelectron Spectroscopy
GCIB: Gas-Cluster Ion Beam